The Astrophysical Journal, 693:1650–1665, 2009 March 10 doi:10.1088/0004-637X/693/2/1650

POWERFUL H_2 EMISSION AND STAR FORMATION ON THE INTERACTING GALAXY SYSTEM Arp 143: OBSERVATIONS WITH *SPITZER* AND *GALEX*

P. Beirão[1], P. N. Appleton[2], B. R. Brandl[1], M. Seibert[3], T. Jarrett[2], and J. R. Houck[4]

[1] Sterrewacht Leiden, Leiden University, P. O. Box 9513, 2300 RA Leiden, The Netherlands

[2] IPAC, California Institute of Technology, Pasadena, CA 91125, USA

[3] Carnegie Observatories, Pasadena, CA, USA

[4] Astronomy Department, Cornell University, 219 Space Sciences Building, Ithaca, NY 14853, USA

Received 2008 October 17; accepted 2008 December 8; published 2009 March 10

ABSTRACT

We present new mid-infrared (IR; 5–35 μm) and ultraviolet (1539–2316 Å) observations of the interacting galaxy system Arp 143 (NGC 2444/2445) from the *Spitzer Space Telescope* and *Galaxy Evolution Explorer*. In this system, the central nucleus of NGC 2445 is surrounded by knots of massive star formation in a ringlike structure. We find unusually strong emission from warm H_2 associated with an expanding shock wave between the nucleus and the western knots. At this ridge, the flux ratio between H_2 and polycyclic aromatic hydrocarbon (PAH) emission is nearly ten times higher than in the nucleus. Arp 143 is one of the most extreme cases known in that regard. From our multiwavelength data, we derive a narrow age range of the star forming knots between 2 Myr and 7.5 Myr, suggesting that the ring of knots was formed almost simultaneously in response to the shock wave traced by the H_2 emission. However, the knots can be further subdivided into two age groups: those with an age of 2–4 Myr (knots A, C, E, and F), which are associated with 8 μm emission from PAHs, and those with an age of 7–8 Myr (knots D and G), which show little or no 8 μm emission shells surrounding them. We attribute this finding to an aging effect of the massive clusters which, after about 6 Myr, no longer excite the PAHs surrounding the knots.

Key words: galaxies: individual (NGC 2444, NGC 2445) – galaxies: interactions – galaxies: ISM – galaxies: starburst – infrared: galaxies

Online-only material: color figures

1. INTRODUCTION

The direct study of warm molecular hydrogen emission from galaxies has been improving considerably through the advent of more sensitive space-borne spectrometers on the *Infrared Space Observatory* (e.g., Rigopoulou et al. 2002; Lutz et al. 2003) and more recently on the *Spitzer Space Telescope*.[5] With the Infrared Spectrograph (IRS[6]) (Houck et al. 2004) on *Spitzer* (Werner et al. 2004) it has been possible to improve upon systematic studies of the mid-infrared (IR) pure-rotational lines of molecular hydrogen in a variety of environments, from nearby normal galaxies (Roussel et al. 2007) to galaxies in more extreme environments, such as groups and clusters (Ogle et al. 2007; Egami et al. 2006; Ferland et al. 2008) and ULIRGS (Armus 2006; Higdon et al. 2005) (see also a review on molecules by Omont 2007).

Recently, unusually strong mid-IR H_2 lines have been discovered in the giant shock-wave structure in Stephan's Quintet (Appleton et al. 2006), and in over a dozen low-luminosity radio galaxies (Ogle et al. 2007, 2008), where H_2 lines are often the strongest in mid-IR wavelengths. Strong H_2 equivalent widths were also found near the "overlap" region in the Antenna interacting galaxy (Haas et al. 2005). These systems have extremely large H_2 equivalent widths and line luminosities ($L_{H_2} > 10^{41}-10^{42}$ erg s^{-1}), and relatively low star formation rates (SFRs). Another defining characteristic is the large ratio of H_2 luminosity to polycyclic aromatic hydrocarbon (PAH) line strength, and the large (0.1%–30%) fraction of H_2 luminosity to the total bolometric luminosity of the objects. Even larger H_2 line luminosities have been found associated with several massive galaxies in X-ray clusters (e.g., Egami et al. 2006). This new class of powerful H_2 emitting galaxy appears to be shock excited, and models of Stephan's Quintet, where a large-scale shock is strongly implicated, suggest that a significant fraction of the bulk kinetic energy in the shock must be funneled into the H_2 line in order to explain the results (F. Boulanger et al. 2008, in preparation; P. Guillard 2008, in preparation). In this context, it is of considerable interest to find other examples of the same kind of emission in nearby systems. This paper describes strong H_2 emission from the strongly interacting galaxy pair Arp 143.

Arp 143 is an interacting pair of galaxies (NGC 2444/2445) with many of the necessary ingredients for a study of shocks generated by galaxy collisions. The southern gas-rich component of the pair, NGC 2445, is notable for the ring of stellar clusters and H II regions, whereas the SO companion is devoid of activity. It is possible that NGC 2445 shares some similarities with collisional ring galaxies (like the Cartwheel ring), because the powerful star forming knots lie along a crescent-shaped wave of H I emission (Appleton et al. 1992), and there is kinematic evidence that the structure is expanding through the disk (Higdon et al. 1997). Early unpublished spectroscopy by Jeske et al. 1986 and optical and near-IR photometry of the knots (Appleton et al. 1992) suggest the star clusters are quite young <30–60 Myr, much younger than the dynamical age of the expanding H I wave—thus providing evidence that they are triggered by a collision with NGC 2444. Jeske et al. (1986) estimated subsolar (LMC-like) metallicity in the disk knots in the range 12+log[O/H] = 8.56–8.77, similar

[5] This work is based, in part, on observations made with the *Spitzer Space Telescope*, which is operated by the Jet Propulsion Laboratory, California Institute of Technology under a contract with NASA. Support for this work was provided by NASA through a GO2 award issued by JPL/Caltech.

[6] The IRS was a collaborative venture between Cornell University and Ball Aerospace Corporation funded by NASA through the Jet Propulsion Laboratory and the Ames Research Center.

to other known collisional ring galaxies (see Bransford et al. 1998). The nucleus has mildly super-solar values of 12+log[O/H] = 9.18—similar to nuclear starbursts.

However, this simple picture is complicated by the unsolved mystery of the large 150 kpc long H I plume (Appleton et al. 1987) which extends just to the north of NGC 2444. The existence of such a long plume implies that the two galaxies involved in the collision have had a previous major tidal encounter in the past (Hibbard & Yun 1999; Hibbard et al. 2000). Perhaps the simplest interpretation of the system is that NGC 2444 may have experienced an initial close passage with NGC 2445 ~100 Myr ago, stripping H I into the plume from NGC 2444. After an initial nonpenetrating encounter, the main stellar body of NGC 2444 has returned to collide recently with the disk of NGC 2445 in a manner similar to collisional ring galaxies (Appleton & Struck-Marcell 1996).

In this paper, we will present new multiwavelength imaging and spectroscopic data of Arp 143, another example of a galaxy with very strong mid-infrared H_2 emission. Our goal is to connect the recent dynamical events in Arp 143 with the shock and star formation history of the galaxy. The paper will use *Spitzer*, *GALEX*,[7] and new ground-based optical and near-IR images as well as mid-IR spectroscopy to explore the physical conditions in Arp 143. This will include the study of the dust and H II region properties, ages and luminosities of star formation regions, and the excitation conditions of the warm H_2 gas. After a description of the images and spectra in Section 2, we will present in Section 3 the multiwavelength photometry and the spectral analysis. In Section 4, the discussion of the results will follow two main directions: the analysis of the shock region using mainly results from the spectral analysis, and the star formation history of the knots based on an interpretation of the ultraviolet (UV)-IR SEDs of each knot. We will assume a distance to Arp 143 of 56.7 Mpc based on its corrected Virgo-centric velocity of 4142 km s^{-1} and an assumed H_0 = 73 km s^{-1} Mpc^{-1}. At this distance, 1 arcsec corresponds to 275 pc.

2. OBSERVATIONS AND DATA REDUCTION

2.1. Spectra

The spectra were taken on 2004 October 24 using the IRS (Houck et al. 2004) on board of the *Spitzer Space Telescope*. All spectral data were processed using IRS pipeline version S15. Figure 1 shows an overlay of the IRS low- and high-resolution slits on a *V*-band image. We have a completely sampled map in the long-low (LL; 15–37 μm) spectral mapping mode, consisting of 17 pointings (each with a 32 s exposure): a total LL exposure time of 544 s. A sparsely sampled map was obtained with short-low (SL; 5–14 μm) which did not fully sample the galaxy as shown in the figure. It consisted of 30 pointings with 61 s exposures each: a total SL exposure time of 1891 s. Since the LL and SL observations are composed of two subslits, each observed separately, convenient off-source "background" exposures were automatically obtained during the observations. These observations were selected to be free of line emission and were subtracted from each on-source exposure.

High-resolution spectra of the nucleus were taken in two nods with two 31 s exposures each for short and long wavelengths (SH and LH), resulting in a total integration time of 248 s. For each module, we averaged the exposures for both nod positions. After the removal of bad pixels, we extracted the spectra for each module, using SMART[8] (Higdon et al. 2004), a tool for the extraction and analysis of *Spitzer*-IRS spectra, written in IDL. For the high-resolution spectra, we did not subtract a background since there was no suitable "sky" spectrum taken. These observations were made early-on in the *Spitzer* mission before it was realized that obtaining a "sky" observation away for the target was useful for rogue-pixel removal (especially LH). Therefore, our SH and LH observations contain low-level zodiacal light in addition to the continuum from the galaxy. This does not affect the measurements of line fluxes (see later) but potentially can affect the measurement of the absolute continuum. The source was sufficiently bright that rogue-pixel removal was not a large issue in the case.

Extraction of all the in-target low-resolution spectra was performed using CUBISM (Smith et al. 2007b), an IDL tool for the construction and analysis of spatially resolved spectral cubes using *Spitzer/IRS* spectra. Bad pixels in the basic calibrated data (BCD) images were manually flagged in each cube pixel, and then automatically discarded when rebuilding the cube.

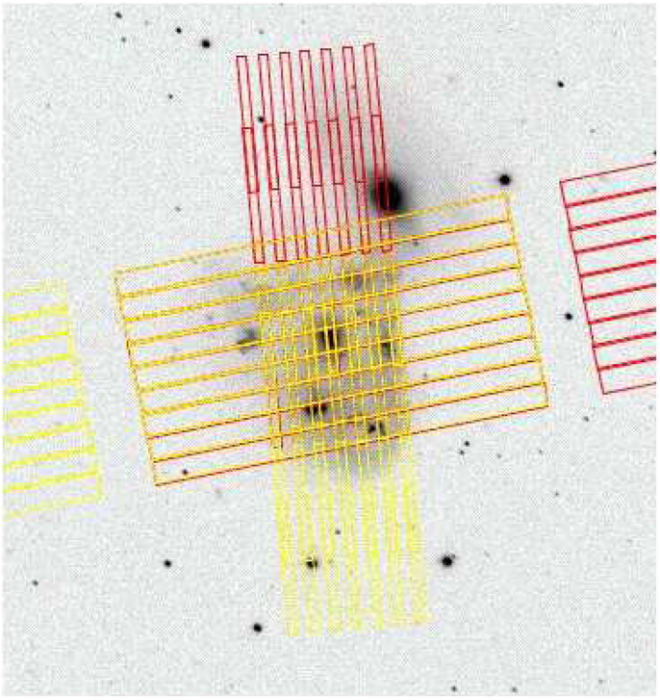

Figure 1. Overlay of the SL (sparse) and LL (complete) maps on a *V*-band image of Arp 143. North is up.

2.2. Images

Figure 2 shows images of Arp 143 at 12 different wavelengths: FUV (λ154 nm) and NUV (λ232 nm) continuum; optical *B*- *V*-, and *R*-band continuum; H_α emission; *K* band, the mid-IR 3.6 μm and 4.5 μm bands, sensitive to the emission of the red stellar population; the mid-IR 5.8 μm and 8.0 μm bands, specially sensitive to PAH and dust emission; and a 24 μm continuum image, built from an IRS LL spectral map. In the FUV image we show the apertures chosen for photometry, matching the main star forming knots visible on FUV, marked from A to G, and the nucleus. Each image was obtained as follows.

[7] *Galaxy Evolution Explorer* (*GALEX*) is a NASA small explorer launched in 2003 April. We gratefully acknowledge NASA's support under Guest Investigator program no. 45.

[8] SMART was developed by the IRS Team at Cornell University and is available through the *Spitzer* Science Center at Caltech.

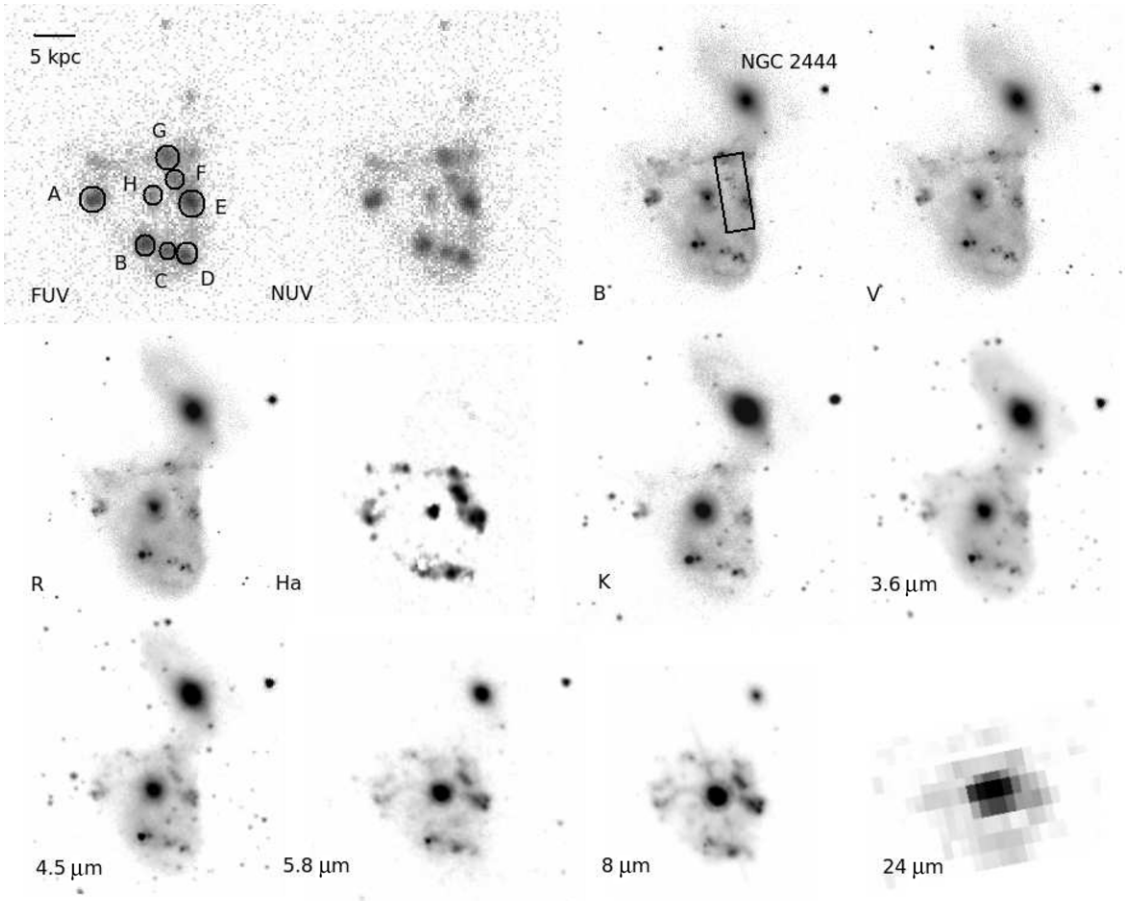

Figure 2. Images of Arp 143 in 12 different bands: *GALEX* FUV, *GALEX* NUV, *B*, *V*, *R*, Hα, *K*, IRAC 3.6 μm, IRAC 4.5 μm, IRAC 5.8 μm, IRAC 8 μm, and IRS LL map at 24 μm. The different apertures used for photometry are overlaid on the FUV image.

2.2.1. FUV and NUV

UV images of Arp 143 were obtained on 2005 January 28 (FUV) and 2006 December 26 (NUV) using the *Galaxy Evolution Explorer* (*GALEX*) satellite (Martin et al. 2005). The galaxy was imaged in the FUV and NUV bands, covering the wavelengths 1344–1786 Å and 1771–2831 Å. The total integration time was 3040 s for the FUV image and 219 s for the NUV. *GALEX* uses two 65 mm diameter, microchannel plate detectors, producing circular images of the sky with 1.2° diameter at 5″ resolution. The *GALEX* image was reduced and calibrated through the *GALEX* pipeline. The fluxes were converted to magnitudes on the AB system (Oke 1990). The data were constructed with version 6 of the *GALEX* pipeline. We co-added two all sky imaging visits to obtain the 219 s of exposure in the NUV image.

2.2.2. Optical and Near-Infrared

We obtained optical images on 2003 February 3 using the Palomar 60″ telescope. The observations were made with a 2048 × 2048 CCD imaging system with a field of view (FOV) of 12.′9 × 12.′9. The pixel scale is 0.″38 pixel^{-1}. The data were taken in three filters, Johnson *B*, Johnson *V*, and Johnson *R*, and exposure times of 500 s for each filter. The night was moonless and transparent and the seeing was 0.″7–1.″0. We used the star RU 152 for calibration. The Hα image was published in Romano et al. (2008) and was taken in the Guillermo-Haro 2.1 m telescope using a narrowband filter centered at 6635 Å (FWHM ∼ 97 Å), which also contains the [N II]λ6583 line. We corrected the Hα flux for [N II] by assuming Hα/[N II]∼ 3, typical of H II regions (Osterbrock 1989). The near-IR images were obtained with good (< 1″) seeing through a K_s ($\lambda = 2.15$ μm) filter using the WIRC camera on the Palomar 200″ telescope in 2004 November 30. WIRC is a 2048 × 2048 pixel wide-field 8.′5 × 8.′5 HgCdTe camera with a pixel scale of 0.″25 pixel^{-1} operated by Caltech.

2.2.3. Mid-Infrared

Arp 143 was imaged with the Infrared Array Camera (IRAC; Fazio et al. 2004) on *Spitzer* at 3.6, 4.5, 5.8, and 8.0 μm on 2005 March 28. The IRAC detectors consist of two 256 × 256 square pixel arrays with a pixel size of 1.″22 resulting in a total FOV of 5.″2 × 5.″2. For each of the four channels, 47 12 s exposures were taken, with a total integration time of 564 s for each channel. The data were reduced using standard procedures (i.e., dark-current subtraction, cosmic-ray removal, nonlinearity correction, flat-fielding and mosaicing) using pipeline version 14.0 of the *Spitzer* Science Center.

3. ANALYSIS

In Figure 3, five low-resolution spectra of 21″ × 21″ regions coinciding with knots B, C, E, F, and the nucleus are shown. In these spectra we can see broad features attributed to PAHs, such as 6.2 μm, 7.7 μm, 8.6 μm, 11.3 μm, and 12.6 μm features. Also noticeable is the distinctive PAH 17 μm complex. In the

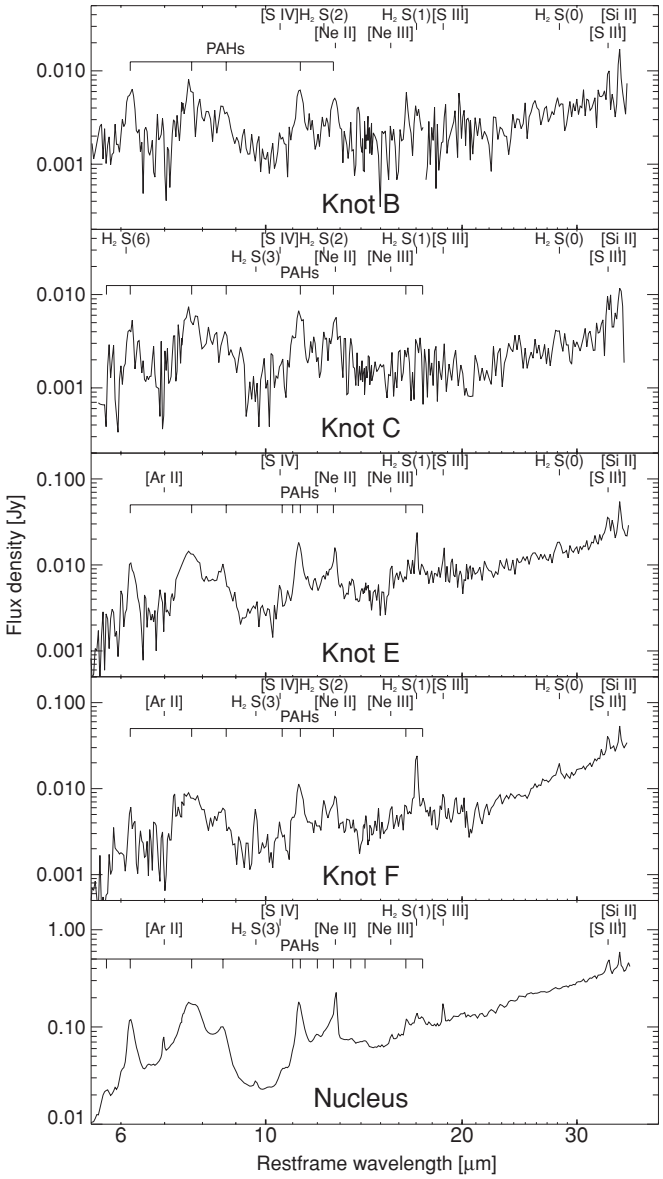

Figure 3. Low-resolution spectra of six regions coinciding with the selected knots.

regions E and F, the H_2 lines at 9.7 μm, 12.2 μm, 17 μm, and 28.2 μm are especially strong. The ionic lines observed are [Ar II] at 6.9 μm, [Ne II] at 12.8 μm, [Ne III] at 15.6 μm, [S III] at 18.8 μm and 33.5 μm, and [Si II] at 34.8 μm. The spectrum of knot D is extremely noisy, and therefore it is not shown in Figure 3. This means that there is no continuum flux detected at this wavelength. However, the PAH features are detected above the sensitivity level. The peak of the 6.2 μm PAH feature, for example, is at 4 mJy, well above the 3σ sensitivity of the SL slit at this wavelength, which is 0.6 mJy. In Figure 4, a low-resolution spectrum from the region where a ring of H I emission was observed by Appleton et al. (1992) and Higdon et al. (1997) is shown, which is delimited in the *B*-band image in Figure 2. This spectrum is very similar to the spectra of knots E and F, but it has some differences. It is even more dominated by distinctive H_2 lines, especially the H_2 S(1) line at 17 μm, although PAH features can also be seen, especially at 11.3 μm. The ionic lines are not so prominent, as the spectrum was taken in a region not dominated by star forming clusters.

3.1. H_2 Lines

Using the pure-rotational H_2 lines, we can probe the physical conditions of the warm molecular hydrogen in the star forming knots. The pure-rotational lines originate from the warm ($T > 100$ K) gas. We measured the H_2 rotational line fluxes using SMART, and derived their excitation temperatures, column densities, and masses of their temperature components. Figure 5 shows the excitation diagrams of the detected H_2 transitions and upper limits for the knots E, F, G, the nucleus, and the ring. Each excitation diagram consist of a plot of the natural logarithm of the column density N divided by the statistical weight g in the upper level of each transition against the upper-level excitation temperature T_{ex}. The column density follows from the Boltzmann equation

$$\frac{N_i}{N} = \frac{g(i)}{Z(T_{ex})} \times \exp\left(-\frac{T_i}{T_{ex}}\right), \quad (1)$$

where $N(i)$ is the molecular column density of the ith transition, N is the total column density of H_2, $g(i)$ is the statistical weight for the ith transition, and $Z(T_{ex})$ is the partition function at the excitation temperature T_{ex}. The values of g for odd and even transitions are different because of the ortho and para transitions. The H_2 line fluxes, and the molecular gas temperatures, column densities, and masses are listed in Table 1.

The excitation temperature of the line-emitting gas is the reciprocal of the slope of the excitation diagram, and corresponds to the kinetic temperature in local thermodynamic equilibrium (LTE). However, the nonlinear decline of $\log(N/g)$ with upper-level energy, commonly seen in shocks within the Galaxy, as well as in external galaxies (Lutz et al. 2003; Rigopoulou et al. 2002), is an indication that no single-temperature LTE model fits these data.

The lowest temperatures are measured in knots E and G, using S(0) and S(1). The temperatures for knots F and H were derived from higher excitation transitions, S(1) and S(2), as S(0) was not detected. The measured temperatures are 137 K for knot E, 280 K for knot F, 178 K for knot G, and 309 K for the nucleus. We can see that the molecular gas is hotter in knot F (280 K) and in the nucleus (309 K), but denser in knot E, where most of the warm molecular gas is concentrated. It is important to note that the temperatures for knots E and G were derived using only the S(0) and S(1) transitions, whereas higher transitions were used in other knots resulting in a higher average temperature of the gas. The derived excitation temperature is also dependent on the ortho-to-para ratio for H_2. During the fit to a multitemperature model through the preferred data points, we constrain the warm gas by the S(0)/S(2) [para] ratio and allowing the higher-order S(3) and S(5) [ortho] transitions to provide a very rough guide to the temperature of a hotter component, resulting in ortho-to-para ratios of 2.2 for knot E, 2.7 for knot G, and $\sim$ 3 for knot F, the nucleus, and the ridge. These ratios agree with LTE models (Burton et al. 1992). The various masses are derived multiplying the column density by the physical area of the aperture corresponding to the knot.

3.2. PAH Features

We used PAHFIT (Smith et al. 2007a) to measure the PAH emission features for each of the knots. Some PAH features are decomposed by PAHFIT into Gaussian components, such as the 7.7 μm and 11.3 μm features, and merged for the calculation of their total flux and EWs. The results of the PAH feature fits are listed in Table 2. Most of the PAH features lie on the SL part

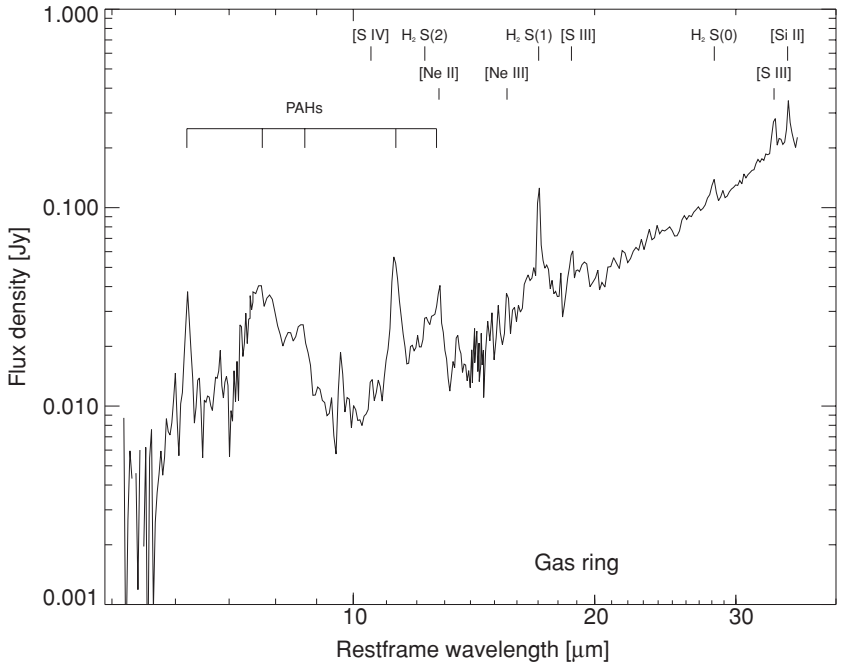

Figure 4. Low-resolution spectrum of the gas ring in NGC 2445.

Table 1
Molecular Hydrogen Line Fluxes (Top Row), Equivalent Widths (Bottom Row), and Diagnostics of the Main Knots[a]

Knot	H_2 S(3)	H_2 S(2)	H_2 S(1)	H_2 S(0)	T (K)[b]	N_{H_2}[c]	M_{H_2}[d]	$L(H_2)$[e]
A	...	...	0.27	0.27	...	...	...	...
B	0.22	0.31	0.39	0.18	...	...	...	...
C	0.33	0.38	0.34	0.50 ± 0.14	...	...	...	...
...	...	...	...	0.604	...	...	...	...
D	0.39	0.38	0.27	0.20	...	...	...	...
E	0.41	0.31	2.48 ± 0.03	1.12 ± 0.08	137	30.6	10.8	1.35
...	...	...	0.335	0.340	...	...	...	...
F	1.85 ± 0.10	1.17 ± 0.21	4.24 ± 0.32	0.88 ± 0.12	280	5.8	0.92	3.11
...	0.386	0.183	1.106	0.194	...	...	...	...
G	0.34	0.32	4.27 ± 0.52	0.70 ± 0.12	178	10.4	3.70	1.78
...	0.355	...	1.285	0.233	...	...	...	...
Ring	3.37 ± 0.34	1.57 ± 0.18	14.5 ± 0.6	5.70 ± 0.69	236	3.1	4.45	7.46
...	0.114	0.027	0.309	0.172	...	...	...	...
Nucleus	1.66 ± 0.05	1.20	3.60 ± 0.15	0.91	309	2.67	0.42	2.13
...	0.022	...	0.030	...	...	...	...	...
Nucleus (high resolution)	...	2.72 ± 0.28	5.94 ± 0.36	0.87	330	1.58	0.60	3.98
...	...	0.008	0.019	...	...	...	...	...

Notes.
[a] Fluxes in units of 10^{-21} W cm^{-2}, and the equivalent widths, below the fluxes, are in μm. Fluxes without errors are upper limits.
[b] Temperatures based on the following slopes: S(0)–S(1) for knot E, S(0)–S(3) for knot F, S(0)–S(1) for knot G, and S(1)–S(3) for the nucleus.
[c] Column densities in units of 10^{19} cm^{-2}.
[d] Warm molecular gas mass in units of 10^7 $M_\odot$.
[e] Luminosities in units of 10^{40} erg s^{-1}.

of the spectrum, meaning that the sparse map only has a 2 pixel wide coverage of the knots. We therefore make an extrapolation of the results taken with these observations to the total area of the knots.

The overwhelming majority of the PAH emission comes from the nucleus, which is also the region with the most emission at 8 μm (Figure 2). From the star forming ring, knots A, C, E, and F have PAH associated with the star clusters. Knot E is the one with the highest PAH emission, and this is also expected from the 8 μm IRAC image in Figure 2.

3.3. Ionic Lines

In Table 3 we present the fluxes of the main ionized gas lines in the low-resolution spectra, as measured using SMART. The errors listed reflect the signal-to-noise ratio (S/N) at the wavelengths where the lines were measured. With these fluxes we calculated the ionic line ratios [Ne III]/[Ne II], [S III]18.7/[S III]33.5 μm, and also [Si II]/[S III].

The [Ne III]/[Ne II] rate, because it is a rate between two ionization states of the same element, it is sensitive to the

Table 2
PAH Fluxes[a] (Top Row) and Equivalent Widths (Bottom Row) in the Main Knots

Knot	6.2 μm	7.7 μm	8.6 μm	11.3 μm	17 μm Complex	11.3/7.7
B	1.186 ± 0.395	1.717 ± 0.466	0.574 ± 0.396	0.567 ± 0.256	0.146 ± 0.103	0.33 ± 0.33
...	1.14	2.49	0.949	1.20	0.045	...
C	0.878 ± 0.229	1.952 ± 0.641	0.371 ± 0.236	0.627 ± 0.128	...	0.32 ± 0.26
...	1.38	3.02	0.652	1.73	...	...
D	0.640 ± 0.359	1.397 ± 0.819	...	0.446 ± 0.392	...	0.32 ± 0.32
...	6.49	11.1	...	2.93	...	...
E	2.083 ± 0.814	5.824 ± 2.675	1.256 ± 0.805	1.503 ± 0.455	0.665 ± 0.632	0.26 ± 0.26
...	4.42	9.03	1.72	1.74	0.756	...
F	0.922 ± 0.304	4.369 ± 0.724	0.734 ± 0.334	0.972 ± 0.184	0.635 ± 0.228	0.22 ± 0.10
...	2.93	9.08	1.26	1.51	1.17	...
G	0.683 ± 0.580	3.98 ± 1.449	0.724 ± 0.416	0.697 ± 0.631	...	0.18 ± 0.18
...	7.89	20.7	1.46	1.25	...	...
Nucleus	22.65 ± 0.441	89.52 ± 0.865	13.39 ± 0.406	15.93 ± 0.312	7.346 ± 0.353	0.18 ± 0.00
...	3.04	14.8	2.12	1.87	0.595	...
Ring	1.14 ± 0.36	4.23 ± 1.62	0.74 ± 0.34	1.04 ± 0.18	0.89 ± 0.31	...
...	1.87	7.97	1.38	1.60	0.94	...

Note. [a] Fluxes in units of 10^{-20} W cm^{-2}.

Table 3
Ionic Line Fluxes and Ratios of the Main Knots[a]

Knot	[S IV]	[Ne II]	[Ne III]	[S III]18 μm	[S III]33 μm	[Si II]	[Ne III]/[Ne II]	[S III]18.7 μm/[S III]33.5 μm	[Si II]/[S III]
A	...	...	0.53	...	0.99 ± 0.09	0.87 ± 0.05	...	...	0.87 ± 0.15
B	0.24	...	0.29	0.43	0.59 ± 0.10	1.16 ± 0.06	...	...	1.97 ± 0.51
C	0.36	...	0.33	0.36	0.43 ± 0.12	0.87 ± 0.11	...	...	1.14 ± 0.90
E	0.90 ± 0.04	2.25 ± 0.09	1.16 ± 0.04	1.24 ± 0.27	2.48 ± 0.29	2.88 ± 0.16	0.52 ± 0.04	0.50 ± 0.19	1.16 ± 0.23
F	0.34 ± 0.02	0.92 ± 0.05	0.62 ± 0.06	0.85 ± 0.19	1.70 ± 0.22	1.64 ± 0.08	0.67 ± 0.11	0.50 ± 0.20	0.96 ± 0.20
G	0.84	0.84	0.90	1.85 ± 0.35	1.38 ± 0.21	2.05 ± 0.25	...	1.34 ± 0.63	1.49 ± 0.48
Nucleus	0.06	30.8 ± 1.36	2.54 ± 0.08	8.71 ± 0.25	14.2 ± 1.2	14.56 ± 1.60	0.08 ± 0.01	0.61 ± 0.08	0.82 ± 0.22
Nucleus (high resolution)	...	63.6 ± 1.6	5.17 ± 0.60	20.7 ± 0.8	28.4 ± 5.3	31.9 ± 1.6	0.08 ± 0.01	0.73 ± 0.20	1.12 ± 0.21
Ring	1.12 ± 0.14	3.29 ± 0.38	0.99	5.21 ± 0.89	10.0 ± 1.12	8.10 ± 0.68	...	0.64 ± 0.15	0.81 ± 0.14

Note. [a] Fluxes in units of 10^{-21} W cm^{-2}.

effective temperature of the ionizing stars, and therefore can be used as a measure of the hardness of the radiation field. This ratio varies typically between 0.05 and 1 in starburst galaxies and H II regions in normal galaxies, and is typically greater than 1 in dwarf galaxies (Thornley et al. 2000). We could only measure the [Ne III]/[Ne II] ratio for knots E, F, and for the nucleus, and the results are 0.52, 0.67, and 0.08. The ratios for knots E and F are compatible with very young massive clusters, and are similar to those found in very young clusters in other interacting systems such as the Antennae, where star forming regions with [Ne III]/[Ne II] ratios between 0.30 and 0.73 are found (Snijders 2007). The ratio for the nucleus is much smaller than the ratios for the ring knots and are similar to the ratios found in the nuclei of starburst galaxies, like NGC 253 (0.07; Devost et al. 2004).

The [S III]18.7/[S III]33.5 μm ratio is a ratio between two lines of the same ionization state, but with different critical densities for collisions with electrons (Osterbrock 1989). Therefore, it is sensitive only to the density of the ionized interstellar medium (ISM). The [S III]33.5 μm line was detected in all knots, but the [S III]18.7 μm was detected only in knots E, F, G, and in the nucleus. As seen in Table 3, the values for [S III]18.7/[S III]33.5 μm ratio for these knots vary between 0.50 in knots E and F and 1.34 in knot G although with a large measurement error for the last case.

The [Si II]/[S III] line ratio is used as a starburst/active galactic nucleus (AGN) diagnostic (Dale et al. 2006). This is because the [Si II]34.82 μm line is a significant coolant of X-ray-ionized regions or dense photodissociation regions (PDRs; Hollenbach & Tielens 1999), more commonly associated with AGN, whereas the [S III]33.48 μm line is a strong marker of H II regions. The typical value found in AGNs is around 3, whereas for nuclear starbursts it is around 1 (Dale et al. 2006). We measured this ratio for all knots, varying from 0.82 ± 0.22 in the nucleus to 1.97 ± 0.51. The low S/N in clusters B, C, and D is reflected in the high errors of the [Si II]/[S III] measurements, and therefore all the values for this ratio are compatible with the values for nuclear starbursts found in Dale et al. (2006).

3.4. High-Resolution Spectrum of the Nucleus

To study the ISM conditions in the nucleus with greater accuracy we took a high-resolution spectrum of the nucleus of NGC 2445, which is presented in Figure 6. We scaled up the SH spectrum by multiplying it by a factor of 1.7 to match the LH spectrum flux at 20 μm. This factor is much lower than the difference between the SH and LH slits, but that is simply due to the fact that the nucleus is practically a point source. The LH and SH spectra were then joined together, resulting in a single

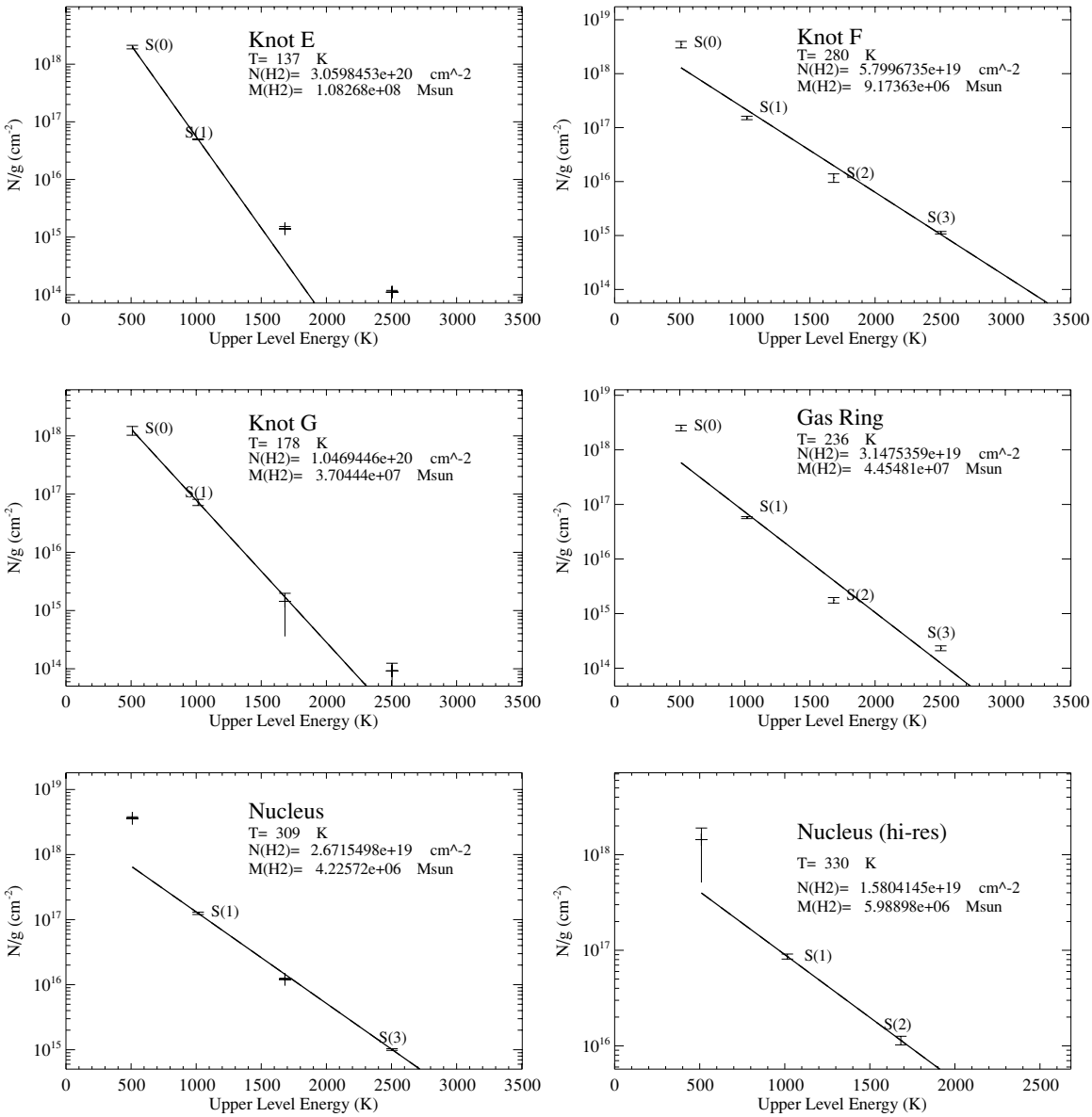

Figure 5. H_2 excitation diagrams for knots E, F, G, the nucleus, and the gas ring. The plots are labeled with the fitting temperatures (T), column densities $N(H_2)$, and molecular gas masses $M(H_2)$ in units of K, cm^{-2}, and $M_\odot$ respectively. The points that are not labeled are upper limits and are not included on the fit.

10–35 μm high-resolution spectrum of the nucleus. The main features present are the ionic lines, such as [Ne II], [Ne III], [S III], and [Si II]. PAH bands are also visible, as the 11.3 μm band and the 16–18 μm feature. Also present are the H_2 rotational lines. These features allow a physical characterization of the ISM of the nucleus, and they can be used to diagnose electron temperature and density and H_2 gas temperature. The measured line ratios are listed in Table 3, along with the lines measured in the same knot using the low-resolution spectrum. We can see that the low-resolution line fluxes have roughly half the flux as the high-resolution lines. This is due to the difference in the extraction apertures. The area of the LH slit is 231 arcsec^2, nearly twice the area of the low-resolution extraction aperture chosen for the nucleus, which is 104 arcsec^2. This gives a ratio of 2.22, whereas the ratio between low- and high-resolution apertures for both the [Ne II] and [Ne III] flux is 2.04, meaning that the surface brightness of the lines decreases with a wider aperture. However, to do a comparison of the continuum fluxes one has to estimate the background flux. We measured the background flux from an off-source SL slit, which gives 116 mJy and 95 mJy for 15 μm and 24 μm, after scaling for aperture sizes. This means that the background accounts for $\sim$ 55% of the high-resolution continuum at 15 μm and $\sim$ 32% of the high-resolution continuum at 24 μm. The ratio of the continuum flux at 15 μm is thus 1.6, meaning that the surface brightness of the warm dust decreases with the aperture. The ratio for the 24 μm continuum is 2.2, meaning that the surface brightness of cooler dust does not vary with slit size.

Comparing the ratios derived from high-resolution with the low-resolution ratios, we find a remarkable match for the [Ne III]/[Ne II] ratio, being 0.08 for both spectra, but for the [S III]18.7/[S III]33.5 μm ratio there are significant differences, being 0.73 for the high-resolution spectrum and 0.49 for the low-resolution spectrum. This reflects the different flux ratios between high- and low-resolution apertures: [S III]18.7 μm has a flux ratio of 2.38 $\pm$ 0.16 thus maintaining its surface

Table 4
Broadband Fluxes of the Main Knots[a]

Knot	R.A. (7 46)	Decl. (+39)	FUV	NUV	*B*	*V*	*R*	*K*	3.6 μm	4.5 μm	5.8 μm	8.0 μm	24 μm[b]
A	58.21 s	00 min 51.24s	0.257 ± 0.005	0.311 ± 0.019	0.504 ± 0.032	0.544 ± 0.035	0.587 ± 0.031	0.761 ± 0.03	0.400 ± 0.172	0.257 ± 0.186	0.878 ± 0.447	1.97 ± 0.74	4.87 ± 1.41
B	55.38 s	00 min 25.75s	0.171 ± 0.003	0.231 ± 0.012	3.17 ± 0.07	3.62 ± 0.08	4.00 ± 0.08	6.18 ± 0.06	2.74 ± 0.32	1.73 ± 0.29	2.03 ± 0.43	2.69 ± 0.65	2.62 ± 0.81
C	54.22 s	00 min 21.25s	0.093 ± 0.002	0.113 ± 0.008	0.323 ± 0.026	0.360 ± 0.029	0.444 ± 0.028	0.644 ± 0.02	0.501 ± 0.274	0.308 ± 0.139	1.14 ± 0.32	2.71 ± 0.54	2.06 ± 0.65
D	53.32 s	00 min 18.25s	0.197 ± 0.003	0.208 ± 0.013	0.632 ± 0.040	0.755 ± 0.041	0.916 ± 0.043	1.25 ± 0.03	0.587 ± 0.200	0.276 ± 0.173	0.604 ± 0.368	0.645 ± 0.597	1.62 ± 0.68
E	52.94 s	00 min 51.25s	0.348 ± 0.005	0.409 ± 0.019	0.754 ± 0.050	0.895 ± 0.042	1.08 ± 0.04	1.39 ± 0.04	0.998 ± 0.246	0.647 ± 0.337	2.78 ± 0.51	6.51 ± 0.84	10.1 ± 1.4
F	53.97 s	01 min 06.25s	0.069 ± 0.002	0.077 ± 0.007	0.120 ± 0.010	0.143 ± 0.012	0.173 ± 0.020	0.309 ± 0.02	0.318 ± 0.142	0.193 ± 0.122	1.10 ± 0.32	2.91 ± 0.55	7.50 ± 0.75
G	54.22 s	01 min 18.25s	0.167 ± 0.004	0.224 ± 0.018	0.636 ± 0.047	0.808 ± 0.040	0.908 ± 0.037	1.25 ± 0.03	$0.560 \pm$	0.335 ± 0.129	0.484 ± 0.279	0.841 ± 0.719	5.47 ± 1.42
Nucleus	55.12 s	00 min 55.75s	0.049 ± 0.005	0.132 ± 0.025	1.41 ± 0.053	2.48 ± 0.064	3.85 ± 0.073	16.5 ± 0.1	10.7 ± 0.6	7.69 ± 0.52	29.5 ± 1.0	87.6 ± 1.8	173 ± 7.14

Notes.
[a] Fluxes in units of mJy.
[b] Errors represent 1σ deviations from the median flux between 22 and 28 μm.

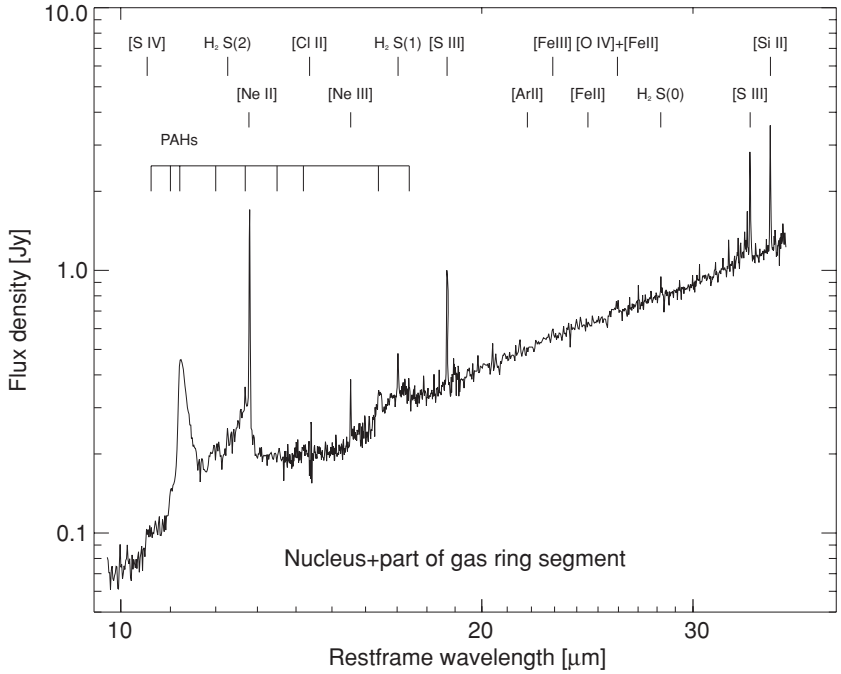

Figure 6. Full high-resolution spectrum of the nucleus of NGC 2445. The SH part was scaled up by 1.8 to match the LH spectrum.

brightness, whereas [S III]33.5 μm has a flux ratio of 1.61 ± 0.09 thus decreasing its surface brightness. This difference possibly reflects a decrease of the ionized gas density as the distance to the nucleus increases. Note that the LH slit could be contaminated by emission form the "shocked" gas region, and thus it can affect the line ratios that use lines [Si II] and [S III]33.5 μm and overestimate the nuclear H_2 component.

3.5. Photometry

Photometry of each knot was performed using *aper*, an IDL tool from the IDL Astronomy Library. We used the FUV *GALEX* image to set an aperture size for each knot, as seen in Figure 2. We used circular apertures of 4.″5 for knots C, F, and the nucleus; 6″ for knots B and D; and 7.″5 for knots A, F, and G. The sky background was determined using circular apertures of the same size as those used to measure each knot. With these apertures, we measured the flux within selected regions inside Arp 143—but avoiding the knots—and averaged the results. We applied extended source corrections for IRAC photometry. These corrections depend on the size of the aperture and do not exceed 6.8%. The resulting fluxes of each of the knots are listed in Table 4.

Arp 143 was not observed with the MIPS instrument at 24 μm. However, in order to allow us to use some of the well-known star formation indicators (e.g., Calzetti et al. 2007) associated with the knots based on MIPS observation, we decided to create pseudo-MIPS 24 μm photometric points by extracting 24 μm data from the full-IRS LL map (see Figure 2, last panel) using the CUBISM-extracted spectra, and the MIPS 24 μm filter response curve. These values are shown in Table 4.

4. RESULTS

Our goal is to characterize the physical origin of the H_2 line emission, its role on the appearance of the ring of star formation around the nucleus of NGC 2445, and describe how the ISM in the knots evolves as they age. To achieve this goal, we now analyze the observations described in the last section according to the following points : (1) the study of the morphology of the system, describing it in the present state, in order to compare it to the present theories on the evolution of ring galaxies; (2) the study of H_2 excitation region and comparison with predictions, in order to study its physical origin; (3) the ISM properties of the knots and its evolution, using the mid-IR spectra to study the ISM in the knots, and UV to *K*-band photometry to study their ages; and (4) the SFRs in the knots, and the future of star formation in the system.

4.1. Morphology

In Figure 7, we present a composite of FUV (blue), *V* band (green), and 8.0 μm emission (red), which traces emission from hot dust. Most of the luminosity in the *V* band comes from the nuclei of the two galaxies, NGC 2444 and NGC 2445, and a ring of star formation knots that surrounds the nucleus of NGC 2445. The nucleus of NGC 2445 dominates the emission in the IR, indicating the presence of large amounts of warm dust, but it also has a large unobscured population of main-sequence and old stars, as it has also significant optical and near-IR components. For a more quantitative comparison, the 8 μm flux from the nucleus is about five times the combined 8 μm flux from the knots. The knots are located along the outer edge of an H I crescent (Appleton et al. 1992). The knots are composed by several massive young clusters, visible in blue, and some are surrounded by PAH emission, visible in red. There are some mid-IR "arms" connecting the nucleus to some of these regions. These arms are connected to the collisional nature of the ring—spokes are expected in gas that is collecting downstream of the ring (Struck et al. 1996). The only other galaxy with similar features reported in the literature is the Cartwheel galaxy (Struck et al. 1996).

NGC 2445 is about 20 kpc across. Some peculiarities reveal a connection between the massive star clusters and the dust, like the easternmost knot at about 12 kpc from the nucleus, identified in the FUV image in Figure 2 as knot A. In Figure 7,

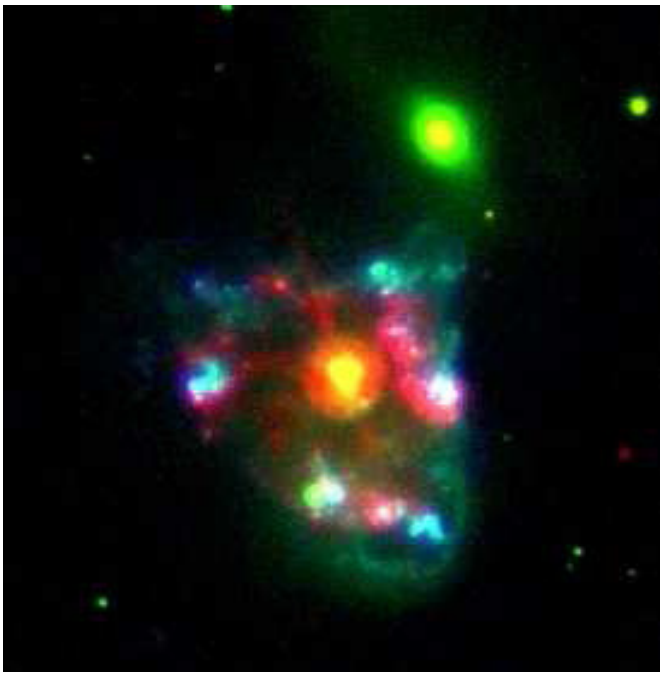

Figure 7. Composite of FUV (blue), *V* band (green), and 8 μm (red) images of Arp 143.

this FUV emitting knot seems to be surrounded by 8 μm mid-IR emission (in red), as it is brighter around the knot and less bright inside a radius of $\sim$ 1 kpc from the center of the knot. This can be interpreted as a shell of warm dust heated by the massive stars. Other knots have 8 μm counterparts, such as knots B, C, E, and F. For knots C and F, the 8 μm emission can be seen at the same site as the optical cluster, whereas in knot E, the 8 μm is found somewhat offset to the SE. Since the 8 μm IRAC band is dominated by PAH emission features, this means that the knots can be divided into two groups: those with associated PAH emission (A, C, E, and F), and "bare" knots, for which little or no PAH counterpart is observed (B, D, and G). This confirms what is observed in the spectra of Figure 3, where PAH features are barely observed in knot D. The nucleus of NGC 2444 also shows substantial 8 μm emission, reflecting substantial massive star formation. The FUV emission comes mainly from knots A, E, and G, showing emission from young massive stars, whereas the IR-bright knot F emits little UV. An even more striking difference between mid-IR and UV brightness, and Figure 2 shows it clearly, is seen in the nucleus, the brightest region in 8 μm, with very little UV emission.

The companion lenticular galaxy NGC 2444 is prominent only in the optical and *K* band, and is rather weak at longer wavelength. This supports the idea that much of the gas has been swept out of the galaxy in the past and it is dominated by an old inactive stellar population. It is possible that a faint "arm" extended from NGC 2444 behind NGC 2445, but this is hard to prove without kinematic data.

4.2. The Shock Front

Rotational emission lines of H_2 may arise through three different mechanisms: UV excitation in PDRs surrounding or adjacent to the H II regions; shocks that accelerate and modify the gas in a cloud, collisionally exciting the H_2 molecules; and hard X-ray photons capable of penetrating the molecular clouds and heating large ionizing columns of gas. Several rotational H_2 lines were detected in the wavelength range of our observations and they are listed in Table 1. Given that these lines trace the molecular gas at different temperatures, studying the spatial distribution of these excitation lines may give us a clue about the main excitation mechanism.

In Figure 8, we present contour maps of the H_2 S(0) (left) and H2 S(1) emission (right) in Arp 143, overlaid on the IRAC 8 μm emission color map. The H_2 emission in Figure 8 is concentrated in two clumps—from the nucleus and in a crescent-shaped ridge (including knot F) west of the nucleus corresponding to the H I crescent seen in VLA observations. The emission is also similar, but not identical to CO (1–0) interferometry distribution (Higdon et al. 1997). These latter observations trace the distribution of cool H_2 emission through collisional excitation of the CO molecule. The main difference between the *Spitzer* (warm) H_2 observations and the CO (cool H_2 tracer) is that the warm gas seems to better define a crescent shape. Indeed, it is precisely here that a shock wave would be expected to heat up the H_2, supported by the fact that the S(1) map more clearly defines the crescent shape than the S(0) line, which is dominated by cooler excitation. This is compatible with the theoretical scenario illustrated in Figure 9, taken from Appleton et al. (1987), which represents the density wave formed after an off-center collision between two galaxies (the site of the collision is marked with an X), which expands outward from the center and also grows in length. It is also worth noting that the area chosen for the spectrum of the gas ring, demarcated in Figure 2, coincides with the area of the shocked H_2 emission. Therefore we can consider this spectrum in Figure 4 as representative of the shocked H_2 region.

The shape of the H_2 emission in Figure 8 is promising but by itself does not settle the case for either PDR or shock

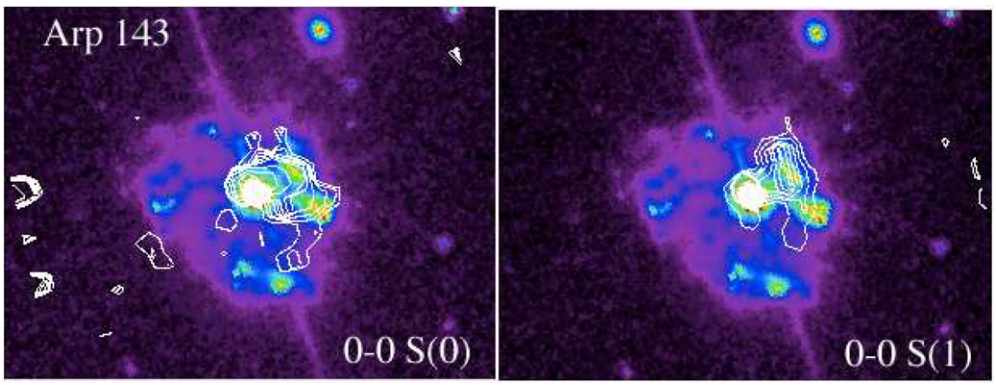

Figure 8. Contour maps of the H_2 S(0) (left) and H_2 S(1) (right) emission in Arp 143, overlaid on an IRAC 8 μm image. Contour levels are at 0.5, 0.6, 0.7, 0.8, 0.9, 1, 1.5, 2, and 3 MJy sr^{-1} for H_2 S(0) and 1, 1.4, 1.8, 2, 2.5, 3, 4, 6, and 8 MJy sr^{-1} for H_2 S(1).

origin. A way to investigate the origin of the excitation of rotational transitions of the H_2 molecule is to make a spatial comparison between the H_2 emission and PAH emission. The H_2 emission-line strength should track the PAH emission line and IR continuum strength in the case where the most common H_2 excitation mechanism is UV excitation at the PDR interface with star formation regions. However, we see a remarkable transition in Arp 143, from the nucleus, where PAH emission is quite strong, to the nonnuclear H_2, which remains strong in the H_2 lines, but is very weak in PAH (and continuum) emission.

Roussel et al. (2007) calculated the logarithm of the average ratio of the power emitted in the sum of the S(0) to S(2) transitions to the power emitted by the PAH features within the IRAC4 band, for H II nuclei and Seyferts from the SINGS survey. The average ratio for H II nuclei -2.19 ± 0.10 and for the Seyferts is -1.80 ± 0.34. We measured these ratios for the knots where H_2 lines from S(0) to S(2) have been measured. We take 7.7 μm and 8.6 μm as the PAH features inside the IRAC4 band. For the nucleus of Arp 143, the ratio is -2.26, which puts it in the average of the H II nuclei. However, for knots E, F, and, G, the ratios are -1.22, -0.90, and -0.94, respectively. This puts them well above the averages for H II nuclei and also for Seyferts. For the gas ring region, which largely coincides with the H_2 crescent, this ratio rises up to -0.36. So, the difference we observe in the H_2/PAH ratio between the nucleus and the ring region in Arp 143 is a strong indication that the H_2 emission ridge seen in Figure 4 is mostly due to shocks. X-ray emission is unlikely to be a strong contribution to the H_2 heating, since the ratio of the [Si II]/[S III] lines in Arp 143 (even in the nucleus) suggests an insignificant contribution to the excitation of [Si II] from X-rays (X-rays can significantly enhance this ratio—as discussed by Dale et al. 2006). This strongly suggests shock excitation within the crescent-shaped structure. A very strong H_2 emission in the absence of strong PAH emission is seen in the shock wave in Stephan's Quintet (Appleton et al. 2006) and in the spectrum of 3C326 (Ogle et al. 2007), where strong shocks are implicated. The lack of a correspondingly large continuum is also one of the characteristics of the shocked H_2 seen in the radio galaxy sample, and the Stephan's Quintet, as well as low-excitation emission lines.

We can interpret the excitation diagrams in Figure 5 also in the context of the different origins of the H_2 emission. The temperatures derived in the excitation diagrams are compatible with either a PDR origin or a shock origin for the H_2 excitation. The H_2 temperature derived for the nucleus is higher than the temperature for the knots associated with the H_2 ridge, and with the H_2 ridge as a whole; still it does not reach the level required to rule out PDR origin, and the comparison with the PAH emission is crucial. However, these temperatures are just average gas temperatures, and the presence of a warmer gas component in the H_2 shock region is possible. The column density of the gas is lower in the H_2 ridge than in the knots, which is expected, since the warm H_2 emission from the ridge is more diffuse, whereas the H_2 emission peak coincides with knot F.

4.3. The Properties of Gas and PAHs in the Knots

The knots in the ring of star formation are very young and are expected to have similar characteristics to young massive clusters discovered in starburst galaxies. We use our observations to study the components of the ISM in these knots, which consist of the molecular gas, ionized gas, and dust.

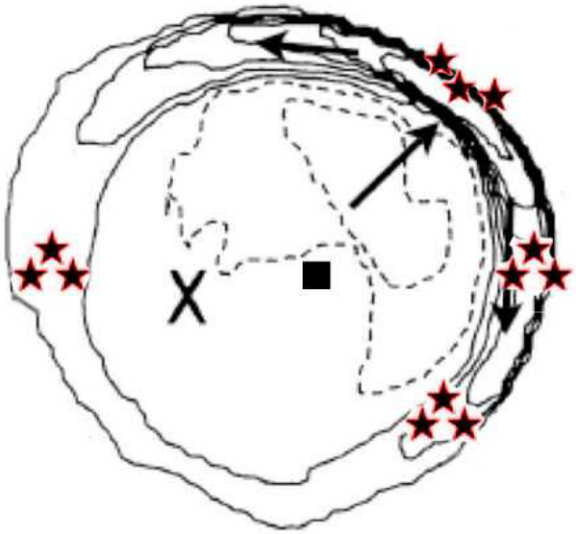

Figure 9. Schematic scenario of NGC 2445 where the knots are situated at the leading edge of the density wave. The contours are from the off-center collision model E from Figure 7 in Appleton & Struck-Marcell (1987), representing a stage of the expansion process of a density wave. The arrows represent the expansion of the wave. Solid contours indicate elevation above the initial unperturbed disk values and dotted contours represent depressed levels. The nucleus is marked with a square. The site of the collision is marked with a cross. (A color version of this figure is available in the online journal.)

The properties of the warm molecular gas, as presented in Section 4.2, can be compared with the properties of the cold molecular gas as studied in Higdon et al. (1997) using CO observations. CO probes molecular gas up to a temperature of 100 K, but provides no information on the "warmer" gas which might be more directly linked to the source of activity. However, we can estimate what fraction of the total gas mass lies in higher temperatures. The fraction H_2 (warm) to H_2 (cool) is 4.8% for knots F and G, 2.6% for the nucleus, but 64% for knot E, assuming a CO–H_2 conversion factor for the LMC. On average, the fraction of warm to cool H_2 amounts to 10%, which is nearly the same found by Rigopoulou et al. (2002) for a sample of starburst galaxies.

Forbidden ionic lines can be used as indicators of the conditions of the ionized gas in the knots and the shock region. The ratio [Ne III]/[Ne II] is used as a measure of electron temperature of the ionized gas; the [S III]18.7/[S III]33.5 μm ratio is used as a measure of electron density. These ratios are compared to modeled ratios derived using photoionization diagnostics by Snijders et al. (2007), assuming Salpeter initial mass function (IMF), stellar mass cutoffs $M_{\rm up} = 100 M_{\odot}$ and $M_{\rm low} = 0.02 M_{\odot}$, and solar metallicity.

From the [S III]18.7/[S III]33.5 μm ratio, we can estimate the density of the knots for which these lines are measured. This ratio is insensitive to the ionization parameter Q and age. As seen in Figure 10 (right), for any Q and age, knots E, F, G, and the nucleus have electron densities in the order of 10^2–10^3 cm^{-3}. This is the average electron density encountered in the center of the starburst galaxy M82 (Förster Schreiber et al. 2001). However Knot E, for example, has a diameter of $\sim$ 1 kpc, about two times the size of the central region of M82 (Beirão et al. 2008), and it is composed of individual clusters that could have much higher densities.

Figure 10 in the left shows the evolution of the model [Ne III]/[Ne II] with age, for a given value of the ionization parameter. Due to difficulties in measuring the [Ne II] line in the low-

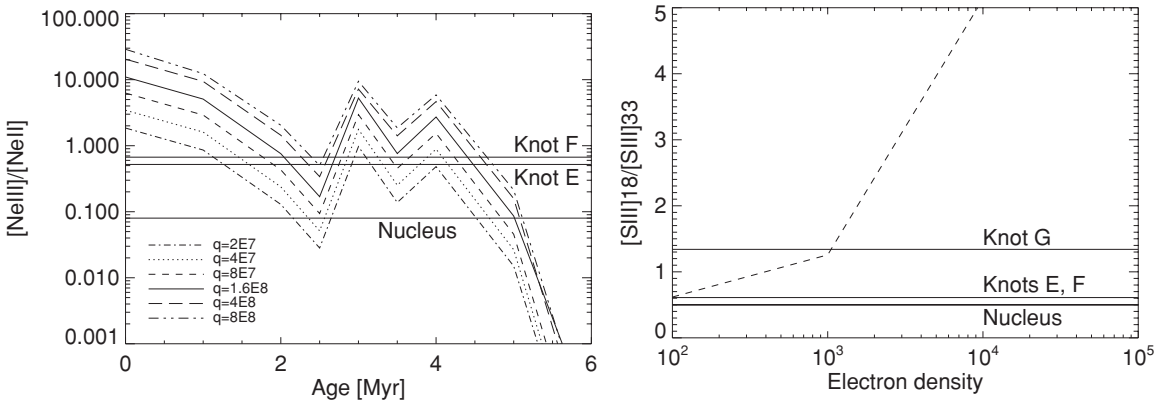

Figure 10. Left: effect of the cluster age on the [Ne III]/[Ne II] ratio. The model curves are computed for a cluster of $10^6 M_\odot$, assuming Salpeter IMF, $M_{up} = 100\ M_\odot$, and $M_{low} = 0.2\ M_\odot$. Each curve represents a different ionization parameter, and the solid curve is the one that approaches the value found in M82 by Förster Schreiber et al. (2001), log $U = -2.3$. The horizontal lines indicate the [Ne III]/[Ne II] for knots E and F, and the nucleus. The first dip in [Ne III]/[Ne II] represents the aging of the stellar population, after which WR stars are produced, increasing the [Ne III]/[Ne II] ratio. The dip at 6 Myr occurs as most massive stars die through supernova explosions. Right: dependence of the [S III]18.7/[S III]33.5 μm ratio on the electron density. The curve is for a single ionization parameter approaching log $U = -2.3$. The horizontal lines indicate [S III]18.7/[S III]33.5 for knots E, F, and G, and the nucleus. Knots E and F have the same value for [S III]18.7/[S III]33.5, which is 0.5.

resolution spectra, as it is merged with a PAH feature at 12.8 μm, we could only measure the ratio for knots E, F, and for the nucleus. We can see that the measured ratios correspond to knot ages of 1–4.5 Myr. The difference in the [Ne III]/[Ne II] ratio between the nucleus (0.08) and the ring knots (0.5-0.7) means that population of recently formed massive stars in the nucleus is older than the young bursts in the ring, having an estimated age of 5–6 Myr. The fit to the low-resolution spectrum of the nucleus gives an A_v of 0.02, which is too low to have any effect on the ratios, and therefore extinction does not affect the ratios significantly.

PAH molecules with different physical characteristics produce different bands. The 6.2 μm, 7.7 μm, and the 8.6 μm bands are produced preferentially by ionized PAHs whereas the 11.3 μm band is produced primarily by neutral PAH molecules. Therefore, the ratio 11.3/7.7 μm may indicate the effect of PAH ionization. We calculate this ratio for all the knots. Given the uncertainties in the PAH flux measurements, we could only derive a reliable 11.3/7.7 μm ratio for knots F and H. We cannot see significant differences between the two ratios, at least not bigger than the uncertainties for knot F.

4.4. The Ages of the Knots

With the fluxes listed in Table 4, we built spectral energy distributions (SEDs) of the main knots, in order to further constrain their physical characteristics. To achieve this, we compare the SEDs with synthetic spectra modeled with Starburst99 (Leitherer & Heckman 1995). There are several parameters we need to consider when fitting the model SEDs to our observations:

1. The mode of star formation. The star formation may occur continuously (continuous star formation (CSF) model) or in a single, almost instantaneous, burst (instantaneous burst (ISB) model). We will adopt the ISB model for the star forming knots, as there is no evidence that star formation has been ongoing for any considerable time in these knots.
2. The stellar IMF. We adopt a Kroupa IMF with an upper-mass cutoff of 100 $M_\odot$ and a lower-mass cutoff of 0.02 $M_\odot$.
3. The initial gas metallicity (Z). We assume subsolar metallicity $Z = 0.4 Z_\odot$, which is similar with the metallicity reported by Jeske et al. (1986).
4. The age of the star clusters. This is a free parameter ranging from 0 to 1×10^9 yr.
5. The effect of extinction. We use the Calzetti starburst extinction law (Calzetti et al. 2000) on the synthetic spectra.
6. Dust emission.

With these conditions, we fitted the synthetic spectra to the measured SEDs of each knot. The fluxes listed in Table 4 were converted to units of erg^{-1} Å^{-1}. We compensated the optical and UV fluxes for a galactic reddening of $E(B - V) = 0.051$, using the extinction maps and laws of Schlegel et al. (1998) and attenuation curve of Cardelli et al. (1989), the latter exclusively for the UV fluxes. Along with a pure stellar synthetic spectrum, the output of Starburst99 includes a nebular emission component as well, which was added to the stellar spectrum for knots C, E, and F. A set of free parameters, such as age, extinction, and continuum flux were adjusted for each knot in order to minimize the χ^2 value. The results are listed in Table 5, as well as the range of parameters within a 95% confidence level. Knot B was left out, as knot B has a foreground star that interferes with the measurements. Although the nucleus could be modeled using the above assumptions, the measured optical to UV flux ratio appears always larger than the modeled spectrum. The variation between subsolar metallicity $Z = 0.4\ Z_\odot$ and solar metallicity does not modify the parameter values significantly.

From the results of the SED fits in Table 5 we can divide the knots in two age groups: knots with ages from 2 to 4 Myr (A, C, E, and F), and knots with ages from 7 to 7.5 Myr (D and G). Given that the interaction occurred 100 Myr ago (Appleton et al. 1987), this age difference is not very significant in terms of the interaction dynamics. Probably due to a clumpy ISM, some clouds collapsed earlier than others, forming stars a little ahead in time than others. The estimated ages come into agreement with Figure 10 (left), which predicted the same range of temperatures for knots E and F.

In Figure 11, we show two examples of SED fittings on knots C (with nebular emission) and D (without nebular emission), being good representatives of the two age groups. We can see how the IRAC 5.8 μm and 8.0 μm fluxes, and the synthetic 24 μm flux, deviate from the pure stellar model for knot D, indicating the presence of PAH and thermal dust emission. We can also see that the SEDs are not easily fitted with a simple instantaneous starburst model, and an example is the excess

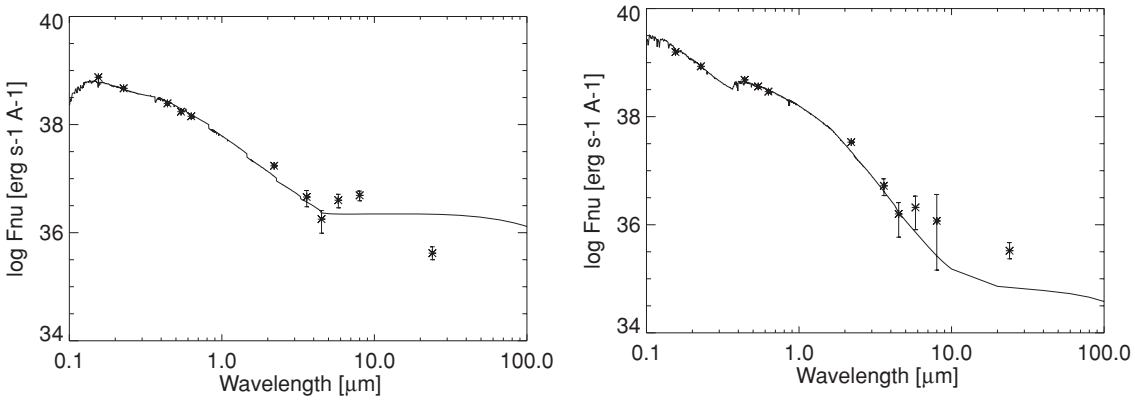

Figure 11. SEDs for knots C (left) and D (right), with Starburst99 synthetic spectra. The error bars represent photometric measurement errors.

Table 5
Properties of Knots Derived from Starburst99 with Best Fit (Upper Row) and 95% Confidence (Bottom Row)

Knot	Age (Myr)	A_v	Mass (10^6 $M_\odot$)
A	3.5	1.0	12.6
	2–4	0.8–1.2	10–15.8
C	3.5	1.5	12.6
	1–5.5	1.1–1.9	7.9–15.8
D	7.5	0.5	12.6
	6.5–8.5	0.4–0.6	10–15.8
E	3.5	1.2	25.1
	3.5–5	1.1–1.4	20–25.1
F	2.5	1.3	6.3
	0.5–6.5	0.8–1.8	4.0–10
G	7.5	0.6	15.8
	6.5–8.5	0.3–0.8	12.6–20.0
Nucleus (ISF)	16	3.0	1122
	15–16	2.6–3.4	1120–1260
Nucleus (CSF)	500	2.7	6.3
	400–800	2.2–3.1	5–7.9

of *K*-band emission in knot C, observed in Figure 11 (left). A *K*-band flux excess was also reported in previous studies that fitted SEDs with Starburst99 (Surace & Sanders 1999 for warm ULIGs; Mazzarella et al. 1992 for the nuclei of Arp 220), which was compensated adding a hot dust (800 K) component contributing to 10%–30% of the emission (Surace & Sanders 1999).

The nucleus of NGC 2445 was modeled using ISF and CSF. CSF is a more reasonable assumption, based on results from ring models, which predict a continuous fueling of the nuclear starburst through gas inflow. In this case, we used a Kroupa IMF with an upper-mass cutoff of 100 $M_\odot$ and a lower-mass cutoff of 1 $M_\odot$. We found that the best fit is achieved for the age of 500 Myr. These ages are radically different from those obtained with [Ne III]/[Ne II] ratios (5–6 Myr), and this is due to the fact that both [Ne II] and [Ne III] lines are produced from the gas excitation by the youngest and hottest massive stars, and that ISF was assumed in the modeling of the lines.

The age determination achieved here is a significant improvement in comparison with past efforts, e.g. Appleton et al. (1992), as their color-based determinations did not include UV bands. The FUV and NUV, as demonstrated here, are essential to the breaking of the age–extinction–metallicity degeneracy.

4.5. Star Formation Rates

With the H_α, FUV, and mid-IR continuum fluxes at 15 μm, 24 μm, and 30 μm, we can derive SFRs for each knot. Using the SFR calibration by Kennicutt et al. (1998), we can derive the SFR from the H_α luminosity, which traces the very young and massive stars. However, the H_α flux is affected by internal extinction, and for the more dusty clusters, we should use the Calzetti calibration law (Calzetti et al. 2007), which includes the 24 μm luminosity to compensate extinction that affects the H_α emission. Far ultraviolet is also a tracer of young massive stars, but even more affected by extinction than H_α. We use here the A_v values in Table 5 to correct the FUV fluxes and the calibration by Salim et al. (2007), which uses *GALEX* FUV calibrations. Mid-IR spectral diagnostics for the SFR were derived in Brandl et al. (2006), based on the fluxes at 15 μm and 30 μm. For each spectrum of the knots, we measured the flux at 14.5–15.5 μm and 29.5–30.5 μm, and calculated the SFRs based on the Brandl et al. (2006) calibrations. In Table 6, we list the corrected FUV, H_α, 24 μm luminosities, as well as the 15 μm and 30 μm fluxes. The SFRs derived using each one of these indicators are also listed.

Adding all the SFRs of the knots, we arrive at a total SFR of 2.16 ± 0.17 $M_\odot$ yr^{-1} from H_α luminosities and 2.40 ± 0.35 $M_\odot$ yr^{-1} using H_α + 24 μm luminosities. This is similar to the 2.5 $M_\odot$ yr^{-1} derived by Jeske et al. (1986) using the H_β fluxes but below the far-IR SFR of 6.21 $M_\odot$ yr^{-1} calculated from IRAS colors (Moshir et al. 1990). It is also far below the SFR derived from the corrected FUV fluxes, which is in total 15.9 $M_\odot$ yr^{-1}.

The SFRs calculated by the Brandl et al. (2006) method are systematically below the SFR calculated using the Calzetti et al. (2007) calibrations, which in turn are below the SFRs derived from FUV. This can be explained by the fact that most of the energy is detected in the optical and not absorbed by dust, which makes this system distinct from more archetypal starbursts like M82. Here, the UV and optical radiation from the clusters is heavily absorbed, making the A_v at least 10 times higher than in Arp 143 (Beirão et al. 2008). This is mitigated in the case of the nucleus, which accounts for $\sim$ 80% of the total 24 μm flux, and thus the discrepancy is smaller. Note that the SFR from UV is heavily dependent on the estimation of A_v, whose values within a 95% confidence can vary by a factor of 2, as seen in Table 5.

5. THE ROLE OF SHOCKS IN THE PROPAGATION OF STAR FORMATION

In the previous sections, we thoroughly discussed the H_2 shocks occurring in NGC 2445 and the ages and densities of the knots that compose the star forming ring. The strong H_2 emission reported this paper exists in and around the density wave, as traced by H I emission shown in Appleton et al. (1992). This is expected from shocks created as the wave moves

Table 6
Star Formation Rates of the Main Knots

Knot	L(FUV)[a]	$L(H_\alpha)$[b]	$L(24\ \mu m)$[b]	$F(15\ \mu m)$[c]	$F(30\ \mu m)$[c]	SFR(FUV)[d]	SFR(H_α)[d]	SFR(H_α+24 μm)[d]	SFR($F(15)$+$F(30)$)[d]
A	1.63 ± 0.10	14.3 ± 0.2	237 ± 11	2.8 ± 1.3	6.7 ± 1.0	1.76 ± 0.06	0.11 ± 0.02	0.11 ± 0.01	0.05
B	...	8.97 ± 1.83	127 ± 6	1.9 ± 0.7	4.0 ± 0.7	...	0.07 ± 0.02	0.07 ± 0.01	0.03
C	1.87 ± 0.04	16.7 ± 2.5	107 ± 5	1.5 ± 0.4	2.7 ± 0.7	2.02 ± 0.04	0.13 ± 0.02	0.11 ± 0.01	0.02
D	0.390 ± 0.006	...	...	1.1 ± 0.1	1.6 ± 0.1	0.419 ± 0.06	...	...	0.012
E	3.49 ± 0.05	45.2 ± 4.1	491 ± 10	4.4 ± 1.1	15.0 ± 1.6	3.77 ± 0.05	0.36 ± 0.03	0.32 ± 0.02	0.10
F	0.880 ± 0.025	27.6 ± 3.2	365 ± 9	3.5 ± 0.9	15.0 ± 0.8	0.951 ± 0.027	0.22 ± 0.02	0.21 ± 0.01	0.10
G	0.421 ± 0.010	12.8 ± 2.2	267 ± 10	2.6 ± 1.9	5.6 ± 1.2	0.463 ± 0.011	0.10 ± 0.02	0.11 ± 0.01	0.04
Nucleus	6.04 ± 0.62	67.9 ± 4.96	8420 ± 363	62.9 ± 1.8	274.9 ± 4.8	6.53 ± 0.67	0.54 ± 0.04	1.46 ± 0.27	1.63

Notes.
[a] Luminosities in units of 10^{28} erg s^{-1} Hz.
[b] Luminosities in units of 10^{39} erg s^{-1}.
[c] Fluxes in mJy.
[d] Star formation rates in $M_\odot$ yr^{-1}.

out through the disk. This is because the gas, unlike the stars in these models, cannot pass through each other and shocks should develop at caustics. In this section, we will discuss the role of these shocks in the development of the knots and its consequences on the morphology of Arp 143.

5.1. The Evolution of PAH Emission with Cluster Age

The SED modeling in this paper provided a further refinement of the age dating of the knots, which is a main advantage over past attempts (Appleton et al. 1992). It showed that not only the H II region nebulosity but also the clusters themselves are consistent with a recent very young burst.

The evolution of PAH excitation with starburst age has been speculated by other studies, like Roussel et al. (2005) in their analysis of dust excitation in NGC 300. We can try to observe this behavior taking advantage of our detailed diagnostics of knot ages.

The improvement on the age dating of the knots allowed us to divide them into two groups: those with an age between 2 and 4 Myr old (knots A, C, E, and F), and those with an age of 7–8 Myr old (knots D and G). What is remarkable is that the younger group of knots corresponds exactly to the knots where PAH counterparts are observed, whereas the older knots are those "bare" of PAHs, as discussed in Section 4.1 and seen in Figure 7. This is the first time this aging effect in star forming galaxies is observed in such chronological detail.

The lack of PAH emission in older knots means that the PAHs have either "cleared out," ceased to be excited, or destroyed during a timescale of 4–5 Myr. The first possibility is that the PAH has been "swept" after $\sim$ 6 Myr by winds from star formation regions. The 8 μm shell in knot A, for example, has $\sim$ 3 kpc in diameter. Assuming a wind velocity of 300 km s^{-1}, the shell has been expanding for 5 Myr, a timescale comparable to the age of the knot. Another possibility could be PAH destruction. Small molecules could become more exposed over time to the hard UV field and are subsequently destroyed, as the dust shell expands and the PDRs become exposed to the outer radiation field. However, both these processes also occur in other galaxies where PAHs are observed at later ages, like the Antennae, so the cause for this behavior resides probably on the nature of the ring galaxy system. Due to the shock wave traced by the H_2 emission, the knots in the ring were formed simultaneously, and therefore we assume an ISB for all the knots. This means that the UV radiation fades away after $\sim$ 6 Myr, and no longer excites the dust surrounding the knot. This can be observed in Figure 10, where the [Ne III]/[Ne II] ratio, a measure of the hardness of the radiation field, decreases dramatically after 6 Myr. The slope of the continuum of knots D and G longward 25 μm indicates the presence of cold dust, meaning that dust is present in these knots, but it is not heated by UV radiation. An older star forming region with continuous burst like the nucleus of NGC 2445 keeps forming new massive stars which continue to excite PAHs and warm up dust. This could also be the origin of the SFR discrepancy seen in Section 4.5, where the SFRs in the knots calculated from the IR continuum are systematically lower than the SFRs calculated from H_α+24 μm luminosities, but not the SFR in the nucleus.

5.2. The H_2 Emission Front and the Simultaneity of Knot Formation

The strong H_2 emission reported this paper traces a density wave expanding outward at a constant speed. In response to the density wave, the knots were formed simultaneously in situ, and that is confirmed by the narrow age range found in Table 6. The fact that the H_2 follows the shape of the H I overdensity is further confirmation that this is a coherent structure.

If we assume the shock velocity from Higdon et al. (1997), 118 ± 30 km s^{-1} and the distance of the clusters to the nucleus, we can calculate the propagation timescale of the shock from the nucleus outward. Given that the knots are on an average distance of 10 kpc, the shock wave has been propagating from the nucleus since 85 Myr ago. However, star formation has been occurring in the nucleus way before then, at least since 300 Myr ago. This is consistent with the kinematic picture first advanced in Appleton et al. (1992): a first interaction with NGC 2444, provoking the onset of star formation in the nucleus 300 Myr ago, and the H I plume observed in Appleton et al. (1987); and a second interaction $\sim$ 85 Myr ago, provoking the emergence of a shock wave which creates a gas overdensity visible in H I (Appleton et al. 1992; Higdon et al. 1997), ultimately leading to a ring of young star forming knots. These knots were created almost simultaneously, and as we have seen, blow out surrounding PAHs in a very short timescale, 5–6 Myr.

Models of ring galaxies have shown the emergence of simultaneous star formation due to an expanding shock wave as a consequence of a head-on collision (Gerber et al. 1996; Struck 1997; Lamb & Hearn 2000). However, the timescales and details, such as gas distribution, frequency of starbursts, etc., are strongly dependent on the position and kinematics of

the galaxies, and there are no models for the particular case of Arp 143.

The future of star formation in the ring of knots will depend on the gas reservoir. Given the mass of atomic and molecular gas, and the SFR for all the knots, we can calculate the duration of star formation in Arp 143 assuming constant SFR. Higdon et al. (1997) found 1.25×10^9 $M_\odot$ of atomic gas in Arp 143, and $2.2 \times 10^9 M_\odot$ of cold molecular gas. Taking the total gas content and an average SFR of 2.16 $M_\odot$, we calculate that the star formation in Arp 143 will last for $\sim$ 2 Gyr. However, the evolution of Arp 143 as a ring galaxy is also likely to increase its SFR, meaning that this is an upper limit for the duration of star formation.

These estimates do not, however, take into account the dynamical evolution of the system. The intruder galaxy, NGC 2444, is likely to swing back and disrupt once more NGC 2445. A dynamical model will be extremely useful to predict the future of star formation in this system, and therefore in similar systems at higher redshifts.

6. CONCLUSIONS

Mid-IR observations of Arp 143 have been presented in this paper, along with ancillary data including *GALEX* UV images. Multiwavelength images from UV to mid-IR show a bright dusty nucleus surrounded by young star forming knots. The four main conclusions of this study are the following.

1. Spectral line maps of the H_2 rotational lines show a ridge of warm H_2 emission that curves between the nucleus and the western knots. The H_2 line flux related to PAH flux is nearly 10 times higher in the ridge than in the nucleus. The flux ratios between the sum of H_2 S(0) and S(2) lines over the sum of PAH 7.7 μm and 8.6 μm lines reveal that this H_2 ridge observed in Figure 8 arises from shocked gas behind the wave that provoked the onset of the ring of star forming knots. This is one of the few cases were this kind of feature is seen.
2. With the use of photometry and fitting the SEDs, we greatly improved the age determination of the knots. The knots in the ring are all very young, varying from 2–7.5 Myr old and the nucleus is about 500 Myr old. The ring of knots is a product of a shock wave that has been expanding from the nucleus since $\sim$ 85 Myr ago, and was formed simultaneously in situ. Behind the shock the molecular gas condenses, and it is traced by the H_2 emission ridge. The improvement of age determination is achieved in this study especially due to the *GALEX* FUV and NUV bands, which are crucial to break the age–extinction–metallicity degeneracy.
3. The distribution of ages of the knots correlates with the presence of PAH emission. Younger 2–4 Myr old knots are associated with PAH emission shells, whereas older 7–8 Myr knots contain little or no PAH emission. The most plausible explanation for this would be an effect of the aging of the massive stars created in a single ISB all over the ring, within a timescale of $\sim$ 6 Myr, after which the UV radiation is no longer energetic enough to excite the PAHs.
4. Given the current reservoir of molecular gas, and assuming that the current SFR maintains itself constant, the star formation in Arp 143 will last for about 2 Gyr. However, as it is very likely that the SFR will increase dramatically, this can only be an upper limit for the duration of the starburst.

We thank Y. Mayya for providing the H_α image. We also thank B. Groves and L. Snijders for making the Starburst99 and Mappings models available. This work is based on observations made with the *Spitzer Space Telescope*, which is operated by the Jet Propulsion Laboratory, California Institute of Technology, under NASA contract 1407.

REFERENCES

Appleton, P. N., Ghigo, F. D., van Gorkom, J. H., Schombert, J. M., & Struck-Marcell, C. 1987, Nature, 330, 140
Appleton, P. N., Schombert, J. M., & Robson, E. J. 1992, ApJ, 385, 491
Appleton, P. N., & Struck-Marcell, C. 1987, ApJ, 318, 103
Appleton, P. N., & Struck-Marcell, C. 1996, FCPh, 16, 111
Appleton, P. N., et al. 2006, ApJ, 639, L51
Armus, L. 2006, ASPC, 357, 218
Beirão, P., et al. 2008, 676, 304
Brandl, B. R., et al. 2006, ApJ, 653, 1129
Bransford, M. A., Appleton, P. N., Marston, A. P., & Charmandaris, V. 1998, AJ, 116, 2757
Burton, M. G., Hollenbach, D. J., & Tielens, A. G. G. M. 1992, ApJ, 399, 563
Calzetti, D., Armus, L., Bohlin, R. C., Kinney, A. L., Koorneef, J., & Storchi-Bergmann, T. 2000, ApJ, 533, 682
Calzetti, D., et al. 2007, ApJ, 666, 870
Cardelli, J. A., Clayton, G. C., & Mathis, J. S. 1989, ApJ, 345, 245
Dale, D. A., et al. 2006, ApJ, 646, 161
Devost, D., et al. 2004, ApJS, 154, 242
Egami, E., Rieke, G. H., Fadda, D., & Hines, D. C. 2006, ApJ, 652, L21
Fazio, G. G., et al. 2004, ApJS, 154, 10
Ferland, G. J., Fabian, A. C., Hatch, N. A., Johnstone, R. M., Porter, R. L., van Hoof, P. A. M., & Williams, R. J. R. 2008, MNRAS, 386, 72
Förster-Schreiber, N. M., Genzel, R., Lutz, D., Kunze, D., & Sternberg, A. 2001, ApJ, 552, 544
Gerber, R. A., Lamb, S. A., & Balsara, D. S. 1996, MNRAS, 278, 345
Haas, M., Chini, R., & Klaas, U. 2005, A&A, 433, L17
Hibbard, J. E., Vacca, W. D., & Yun, M. S. 2000, AJ, 119, 1130
Hibbard, J. E., & Yun, M. S. 1999, AJ, 118, 162
Higdon, J. L., Rand, R. J., & Lord, S. D. 1997, ApJ, 489, L133
Higdon, J. L., et al. 2004, PASP, 116, 975
Higdon, J. L., et al. 2005, ApJ, 626, 58
Hollenbach, D. J., & Tielens, A. G. G. M. 1999, RvMP, 71, 173
Houck, J. R., et al. 2004, ApJS, 154, 18
Jeske, N. A. 1986, PhD thesis, Univ. California, Berkeley
Lamb, S. A., & Hearn, N. C. 2000, in ASP Conf. Ser. 215, Cosmic Evolution and Galaxy Formation: Structure, Interactions, and Feedback, The 3rd Guillermo Haro Astrophysics Conference, ed. J. Franco, L. Terlevich, O. Lopez-Cruz, & I. Aretxaga (San Francisco, CA: ASP), 291
Leitherer, C., & Heckman, T. 1995, ApJS, 96, 9
Lutz, D., Sturm, E., Genzel, R., Spoon, H. W. W., Moorwood, A. F. M., Netzer, H., & Sternberg, A. 2003, A&A, 409, 867
Kennicutt, Jr, R. C. 1998, ApJ, 498, 541
Martin, D. C., et al. 2005, ApJ, 619, L1
Mazzarella, J. M., Soifer, B. T., Graham, J. R., Hafer, C. I., Neugebauer, G., & Matthews, K. 1992, AJ, 103, 413
Moshir, M., et al. 1990, IRAS Faint Source Catalogue, version 2.0 (Pasadena, CA: JPL)
Ogle, P., Antonucci, R., Appleton, P. N., & Whysong, D. 2007, ApJ, 668, 699
Ogle, P., Antonucci, R., Leipski, C., Appleton, P., & Whysong, D. 2008, in ASP Conf. Ser. 386, Extragalactic Jets: Theory and Observation from Radio to Gamma Ray, ed. T. A. Rector & D. S. De Young (San Francisco, CA: ASP), 15
Oke, J. B. 1990, AJ, 99, 5
Omont, A. 2007, RPPh, 70, 1099
Osterbrock, D. E. 1989, Astrophysics of Gaseous Nebulae and Active Galactic Nuclei (Mill Valley, CA: Univ. Sci. Books)
Rigopolou, D., Kunze, D., Lutz, D., Genzel, R., & Moorwood, A. F. M 2002, A&A, 389, 374
Romano, R., Mayya, Y. D., & Vorobyov, E. I. 2008, AJ, 136, 1259
Roussel, H., Gil de Paz, A., Seibert, M., Helou, G., Madore, B. F., & Martin, C. 2005, ApJ, 632, 227
Roussel, H., et al. 2007, ApJ, 669, 959
Salim, S., et al. 2007, ApJS, 173, 267
Schlegel, D. J., Finkbeiner, D. P., & Davis, M. 1998, ApJ, 500, 525
Smith, J. D., et al. 2007a, ApJ, 656, 770
Smith, J. D. T., et al. 2007b, PASP, 119, 1133

Snijders, L. 2007, PhD thesis, Leiden University
Snijders, L., Kewley, L. J., & van der Werf, P. 2007, ApJ, 669, 269
Struck, C. 1997, ApJS, 113, 269
Struck, C., Appleton, P. N., Borne, K. D., & Lucas, R. A. 1996, AJ, 112, 1868
Surace, J. A., & Sanders, D. B. 1999, ApJ, 512, 162
Thornley, M. D., Förster Schreiber, N. M., Lutz, D., Genzel, R., Spoon, H. W. W., Kunze, D., & Sternberg, A. 2000, ApJ, 539, 641
Toomre, A., & Toomre, J. 1972, ApJ, 178, 623
Verontsov-Velaminov, B. A. 1959, Atlas and Catalogue of Interacting Galaxies. Part I (Moscow: Moscow Univ. Press)
Werner, M. W., et al. 2004, ApJS, 154, 1